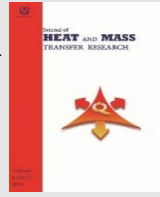




Semnan University



Research Article

A Study on the Reduction of Drag and Heat Transfer on a Conventional Hypersonic Nose Cone

Mohammad Hadi Eslamy ^{a*}, Mohsen Sargolzayi ^a, Esmail Yadollahi afra ^b

^a Qadr Aerodynamic Institute, Imam Hossein University, Tehran, 1698715461, Iran (kpeslamy@ihu.ac.ir)

^b Department aerospace engineering, faculty of new sciences and technologies, Semnan University, Semnan, 19111-35131, Iran

ARTICLE INFO

Article history:

Received: 2023-10-19

Revised: 2024-03-22

Accepted: 2024-05-12

Keywords:

Single-Cone Nose;

Double-Cone Nose;

Stanton Number;

Pressure Distribution;

Drag Coefficient.

ABSTRACT

In the present study, the effect of jet injection on two geometries—single-cone and double-cone—subjected to hypersonic flow is investigated. The simulations are performed using ANSYS-Fluent software. The baseline case is one where the nose lacks injection. The single-cone nose is tested at Mach 6, and the double-cone nose at Mach 5.4. The results show that increasing injection pressure results in a drag coefficient reduction of 49.2% for the single-cone geometry and 62.7% for the double-cone geometry, compared to the baseline. Additionally, the heat flux decreases by 60% for the single-cone nose and 41.3% for the double-cone nose. Higher injection pressure leads to an increase in bow shock standoff distance upstream of both the single-cone and double-cone noses. Increasing injection temperature has minimal impact on the drag coefficient and pressure distribution on the surface of the single-cone nose but significantly reduces the Stanton number, thereby decreasing heat transfer and enhancing nose cooling. Increasing the injection diameter from zero to 5 mm in the single-cone nose results in a 23% reduction in drag coefficient, while for the double-cone geometry, increasing the diameter to 16.5 mm reduces the drag coefficient by 75.04%. Changing the fluid type from air to a gas mixture decreases the maximum Stanton number by 19.3%.

© 2025 The Author(s). Journal of Heat and Mass Transfer Research published by Semnan University Press.

This is an open access article under the CC-BY-NC 4.0 license. (<https://creativecommons.org/licenses/by-nc/4.0/>)

* Corresponding author.

E-mail address: kpeslamy@ihu.ac.ir

Cite this article as:

Mohammadi, A. and Mahdi-Nia, M., 2025. Title of article. *Journal of Heat and Mass Transfer Research*, 12(2), pp. xx-xx.

<https://doi.org/10.22075/JHMTR.2024.39315.2050>

1. Introduction

The high-altitude and high-speed flight of spacecraft has led to extensive research on the aerodynamics of flying bodies at hypersonic speeds. Hypersonic flow, typically characterized by a Mach number greater than 5, is associated with unique physical phenomena such as ionization, extreme wave drag, aerodynamic heating, and intense flow gradients. Among these, heat transfer and drag reduction are the most critical challenges to address. Drag control is primarily influenced by the aerodynamic design of the body, while aerodynamic heating is governed by flow turbulence and chemical reactions in the air. Although numerous studies have been conducted to calculate aerodynamic heating and wave drag in hypersonic regimes [1], computational limitations have restricted the exploration of unsteady hypersonic flow regimes. This paper focuses on the use of counterflow jet injection as a method to simultaneously reduce aerodynamic heating and drag force in hypersonic flows.

1.1. Methods for Drag and Heat Flux Control

Various methods have been proposed to control drag and heating in supersonic and hypersonic flows. These include thermal shields [2], aerospikes [3], jet injection [4, 5], cavities [6], energy discharge [7], and combined methods such as jet injection with cavities [8] or aerospikes with transverse gas injection [9]. Each method has its advantages and limitations. For instance, energy discharge effectively reduces drag but has minimal impact on heat flux reduction. Cavities are effective in controlling heat flux but may increase drag in certain scenarios. Thermal shields, while useful, are limited by their weight and operational duration. Aerospikes, though simple to install, suffer from rapid degradation at high temperatures. Among these, counterflow jet injection has emerged as a promising technique due to its potential to address both drag and heating challenges simultaneously.

1.2. Counterflow Jet Injection: Mechanisms and Challenges

Counterflow jet injection involves injecting a gas through a narrow channel on the body into the external flow. This method requires careful consideration of internal flow dynamics, including flow dilution [10, 11], proper mixing [12, 13] to control gas temperature, and nozzle design to achieve appropriate velocity, pressure, and temperature for injection [14, 15]. The external flow interaction with the injected jet is critical for achieving drag and heat flux reduction.

Studies have shown that the effectiveness of counterflow jets depends on parameters such as jet diameter, pressure ratio, injected gas type, and free stream Mach number.

1.3. Numerical and Experimental Studies on Counterflow Jets

Numerous studies have investigated the performance of counterflow jets in hypersonic flows. Guo et al [16] studied the effects of opposing jet layout on a hypersonic flow passing a blunt body. They mentioned that in comparison with the no jet case, the counter jet pushes the detached shock wave upstream greatly. The oblique jet layout also can push the detached shock wave upstream for a long distance, and two jet layers are generated symmetrically in the flow field. Huang et al. [17] demonstrated that increasing the jet diameter decreases the critical pressure ratio, while larger body diameters improve temperature control efficiency. wang et al [18] show that a single pressure parameter can control the formation of a supersonic opposing jet to form a long penetration mode and a short penetration mode. The ratio of the ambient pressure to the jet pressure at the stagnation point of the blunt body can directly affect the flow field structure of the opposing jet, and reasonable control of opposing jet parameters is an effective way for thermal protection and drag reduction of blunt body structures. Jin [19] found that counterflow jets perform better at higher free stream Mach numbers, particularly under lower pressure ratios. Yuan et al. [20] highlighted the importance of jet exit velocity, showing that a velocity of 200 m/s can reduce the heat transfer coefficient by up to 36%. Shen et al. [21] compared the effectiveness of different gases, with helium achieving the highest efficiency (85.1%) in reducing aerodynamic heating. Gao et al. [5] confirmed that increasing jet pressure enhances penetration into the counterflow, thereby reducing surface temperature. Li et al. [22] explored the effect of multiple jets, finding that increasing the number of jets (up to 9) significantly reduces aerodynamic heating and drag. Gorderodbari et al. [23] emphasized the role of injected gas type and pressure, noting that higher injection pressures improve cooling efficiency. Zhu and Ji [4] identified the critical jet pressure for maximum drag reduction (32.6%) at Mach 2.5. Yixing [24] introduced a dimensionless parameter combining mass flux and jet pressure ratio, showing a 20% drag reduction at Mach 3.98. Gardaroodbari et al. [25] compared helium and carbon dioxide, with helium proving more effective in reducing thermal load. Chen et al. [26] used LES to study jet penetration states, distinguishing between long and short

Table 1. Summary of Research Studies

Ref.	year	M_∞	M_j	$T_{0,j}(K)$	AOA (deg)	gas	Geometry layout	Numerical Simulation	experimental	Drag Reduction	Heat Flux Reduction
[16]	2019	6	1.5	300	0	Air	Hemisphere	■	□	■	■
[17]	2019	---	1	---	0	---	Hemisphere and Cone	■	□	□	■
[18]	2019	10	---	300	0	Nitrogen	Apollo	■	□	□	■
[19]	2019	6	1	300	0	Air	Hemisphere	■	□	□	■
[5]	2018	---	---	---	0	Air	Hemisphere	■	□	□	■
[20]	2016	6	1	300	0	Air	Wave Rider	■	□	■	■
[21]	2015	9.5	1	300	---	----	Blunt Nose Cone	■	□	□	■
[4]	2014	5.2	1	---	---	Air	Hemisphere	■	□	■	□
[22]	2013	3.98	1	300	0	N2	Hemisphere	■	□	■	□
[23]	2012	5.75	1	300	0	----	Reentry Capsule	■	□	□	■
[24]	2011	2.5	---	294	0	Air	Hemisphere	■	□	■	□
[25]	2011	6.5	1	300	---	Air	Ogive Nose	■	□	■	■
[26]	2011	5.8	---	---	0	---	Hemisphere	■	□	■	■
[27]	2010	---	1	300	0	---	Two Geometries	■	□	■	■
[28]	2009	8	---	---	0	---	Reentry Capsule	□	■	□	■
[29]	2009	8	---	---	0	---	Reentry Capsule	□	■	■	□
[30]	2009	5.9	---	---	0	---	Reentry Capsule	□	■	□	■
[31]	2007	---	---	300	0,10	---	Apollo	■	□	■	■

1 penetration modes based on pressure ratios.
 2 Anjalidowi and Aruna [27] examined critical jet
 3 parameters at Mach 5.6, observing that
 4 increasing jet pressure reduces frictional drag,
 5 total drag, and heat transfer. Shah et al. [28]
 6 categorized jet structures into four regions based
 7 on pressure ratios, highlighting the transition
 8 between short and long penetration states.
 9 Tamada et al. [29] compared supersonic and
 10 hypersonic flows, showing that short penetration
 11 occurs at lower pressure ratios in hypersonic
 12 regimes. Kulkarni and Reddy [30, 31]
 13 experimentally demonstrated significant heat
 14 transfer reduction (45%) and drag reduction
 15 with increasing jet pressure ratios. Sreeram and
 16 Jagadesh [32] found that heavier gases like
 17 nitrogen reduce heat transfer more effectively
 18 near the stagnation point, while helium performs
 19 better farther from it. Cheng et al. [33] showed
 20 that counterflow jets lose effectiveness at non-
 21 zero attack angles.

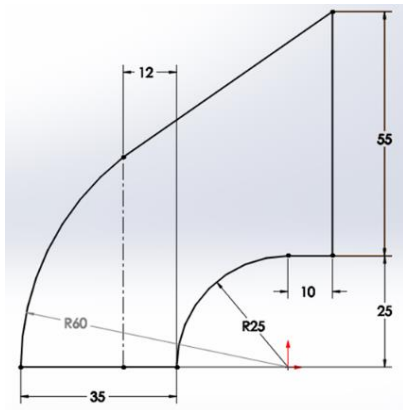
22 1.4. Critical Analysis and Research Gaps

23 While significant progress has been made in
 24 understanding counterflow jet dynamics, several
 25 gaps remain. For instance, the transition between
 26 jet-off and jet-on states, flow field oscillations,
 27 and the stability of jet structures at varying
 28 pressure ratios require further investigation.
 29 Additionally, the combined effects of multiple jets
 30 and the influence of different gas types on jet
 31 penetration and cooling efficiency need deeper
 32 exploration. The present study aims to address

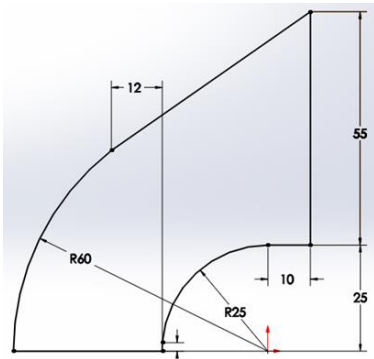
33 some of these gaps by focusing on the external
 34 flow interaction of counterflow jets and their
 35 simultaneous impact on drag and heat flux
 36 reduction. Table 1 summarizes the
 37 aforementioned studies. In the present article,
 38 the geometry and numerical model are first
 39 described. Then, the validation of the solution,
 40 mesh independence, and y^+ examination are
 41 conducted. The next section investigates the
 42 effects of injection pressure ratio, jet diameter,
 43 injection temperature, and the type of injecting
 44 fluid within the computational domain. The
 45 changes in shock position, pressure distribution,
 46 temperature, and Mach number near the nose are
 47 examined. Subsequently, the geometry of the
 48 dual-conical configuration is analyzed in both
 49 non-injection and injection scenarios. In this
 50 context, the effects of jet diameter and injection
 51 pressure ratio on the flow characteristics near
 52 the nose, as well as the position and structure of
 53 the shock wave, are studied. In the conclusion
 54 section, a summary of the main achievements of
 55 the paper is presented, and suggestions for future
 56 work are proposed.

58 2. Geometry and Numerical Model

59 The two-dimensional geometric model used
 60 in this paper is shown in Figure 1. According to
 61 Figure 1 (a), the geometry consists of a quarter-
 62 circle nose with a radius of 25 mm, followed by an
 63 extension of 10 mm. In Figure 1 (b), the
 64 counterflow jet is installed in front of the blunted
 65 body, with a jet diameter of 2 mm. The selected
 66 geometry is adapted from reference [34].



a) Without Jet Injection



b) With Jet Injection

Fig. 1. Dimensions of the Solution Field [34]

The Mach number, static pressure, static temperature, and angle of attack for the free stream, along with the Mach number, stagnation pressure, and stagnation temperature for the counterflow jet, are presented in Table 2.

Table 2. Specifications of Free Stream and Jet

Free stream conditions	Injection conditions	Wall conditions
Air	Nitrogen	$T_w = 295$ K
$Ma_\infty = 3.98$	$Ma_j = 1$	No Slip
$P_{0\infty} = 1.37$ MPa	PR = 0.2-0.8	
$T_{0\infty} = 397$ k	$T_{0j} = 300$ k	

The initial wall temperature is set to 300 K, and the airflow is considered as an ideal gas. Figure 2 shows the structured mesh generated using ICEM software and the boundary conditions. The boundary conditions include axis (axisymmetric), far-field, pressure outlet, and pressure inlet (counterflow jet boundary condition). The k- ω SST turbulence model is selected. In this paper, the Reynolds Averaged Navier Stokes (RANS) equations are solved to obtain heat load and drag coefficient values. The implicit AUSM scheme is used for flux calculation, which is suitable for capturing sharp gradients like shock waves in supersonic/hypersonic flows.

Second-order spatial discretization accuracy is considered.

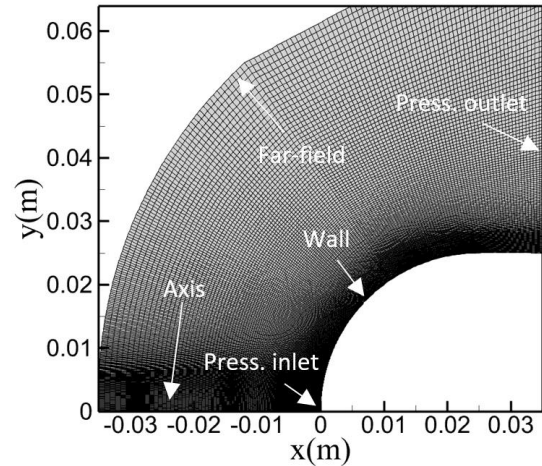
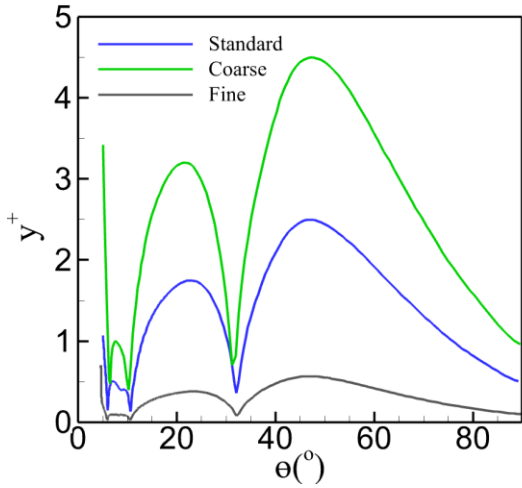


Fig. 2. Structured Mesh of the Computational Domain

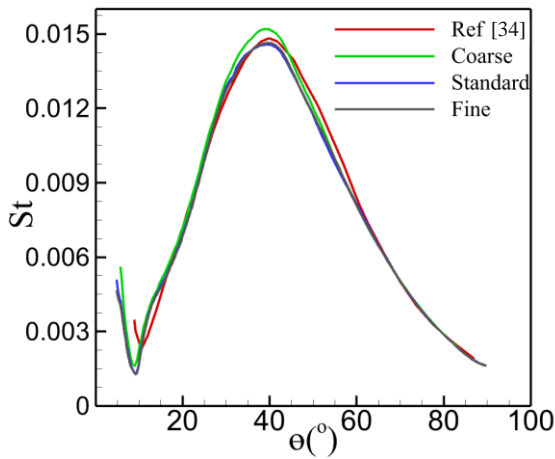
3. Validation and Grid Independence

3.1. Grid Independence

To ensure the accuracy of the numerical simulations, the study performs validation using a grid independence study. The grid independence study examines different mesh resolutions to ensure that further refinement does not significantly alter the results. For the validation model, three meshes were used: coarse, standard, and fine. The coarse mesh includes 27,200 cells, the standard mesh includes 80,876 cells, and the fine mesh includes 114,000 cells. To apply the boundary layer mesh on the model surface for increased accuracy, the height of the first cell is calculated to maintain a y^+ value of around 3, and then the mesh is refined near the surface, especially close to the nose, to accurately simulate regions with high gradients. The y^+ values for these three meshes are presented in Figure 3a. It can be observed that the y^+ values for the standard and fine meshes are appropriate. The results for the Stanton number distribution on the surface under the mentioned flow conditions are presented in Figure 3b. Based on the graph, it is observed that the y^+ results for the standard mesh do not differ significantly from the fine mesh. In other words, refining the mesh further does not change the results, indicating that the results obtained with the standard mesh are grid-independent. Therefore, the standard mesh with 70,876 cells will be used in the remainder of this paper.



a) The Range of y^+ for Three Different Meshes



b) Variations of the Stanton Number on the Nose as a Function of the Angle θ

Fig. 3. y^+ and Stanton number

3.2. Validation

Two parameters, drag force and aerodynamic heating, are very important in this research. Drag force is the result of pressure distribution on the surface and to study this parameter, pressure distribution on the surface has been studied under different conditions. Also, the heat flux generated on the surface is presented with Stanton number (St). Stanton number represents the heat flux generated on the surface. The Stanton number is a dimensionless parameter used to measure heat transfer between a surface and the surrounding fluid. It represents the ratio of convective heat transfer to thermal energy capacity in the fluid. In this paper, the Stanton number is used to evaluate the effectiveness of jet injection in reducing heat transfer on hypersonic nose geometries. Stanton number is calculated using the following formula:

$$St = \frac{q_w}{(T_{aw} - T_{wall})\rho_\infty c_{p_\infty} u_\infty} \quad (1)$$

In the above formula q_w represents heat transfer, ρ_∞ is the free stream density, c_{p_∞} is the specific heat capacity, u_∞ is the free stream velocity, T_{wall} is the wall temperature and T_{aw} is the adiabatic wall temperature. Due to viscous dissipation (friction between adjacent layers of the fluid), a region with high temperature changes forms within the boundary layer. The high-temperature fluid within the boundary layer transfers heat to the body until the temperature gradient at the wall becomes zero. This temperature is called the adiabatic wall temperature T_{aw} and is calculated using the following formula:

$$T_{aw} = T_\infty \left\{ 1 + \sqrt[3]{pr} \left[(\gamma - 1) / 2 \right] M_\infty^2 \right\} \quad (2)$$

In this relation, T_∞ is the free stream temperature and M_∞ is the free stream Mach number. The Prandtl number (pr) is 0.71, γ , the ratio of specific heats, is 1.4. The boundary conditions considered in this section are similar to those stated in reference [32]. Given the significant temperature variations in the flow field, the parameters Cp and k are considered as functions of temperature. Therefore, these parameters cannot be assumed constant and must change with temperature. The results for the Stanton number distribution on the surface, considering compressibility effects for both constant and temperature-dependent Cp and k, are shown in Figure 4 and compared with the reference [34]. For constant values of Cp and k, there are differences between the present study and the reference [34] in the range of 30 to 40 degrees. However, when Cp and k are considered variable, the results show excellent agreement.

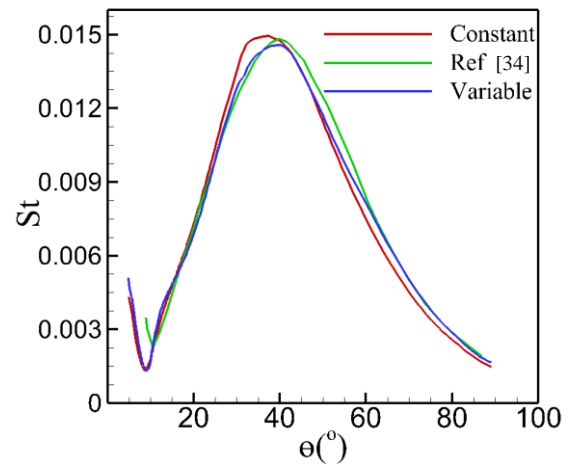


Fig. 4. Variations of the Stanton Number on the Nose as a Function of the Angle θ for Constant and Temperature-Dependent Values

1 4. Results

2 In this section, the results of the numerical
3 simulation are examined. As stated in the
4 previous sections, various parameters play a role
5 in drag reduction and heat transfer, each of which
6 will be analyzed in this section.

7 The most important parameter that has the
8 greatest effect on drag reduction, based on
9 studies, is the jet injection pressure ratio. The
10 geometry under study is the same hemisphere
11 geometry described in section 2 (Figure 1). The

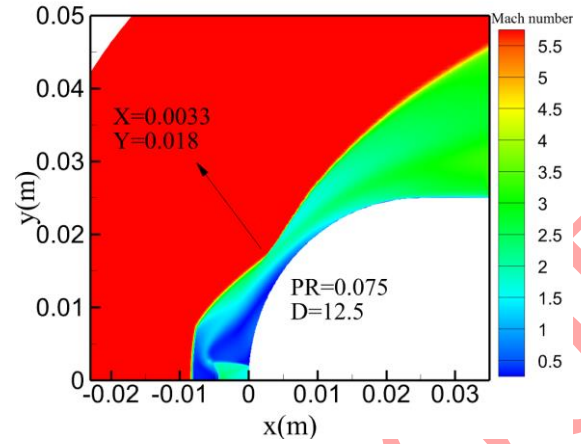
12 boundary conditions for the free stream are
13 fixed with a Mach number $M_\infty=6$ stagnation
14 pressure $P_\infty=4020$ kPa, and stagnation
15 temperature $T_\infty= 1812$ K. Additionally, injection
16 pressures of 301.5, 402, 603, 804, and 1005 kPa
17 are considered to examine the jet injection
18 pressure. In all these cases, the ratio of the jet
19 orifice diameter to the body diameter ($D=d_b/d_j$)
20 is 12.5, and the total jet temperature T_{0j} is 900 K.

21 Figure 5 shows the Mach number contours at
22 injection pressure ratios ($PR = P_{jet}/P_\infty$) of
23 0.075, 0.1, 0.15, 0.2, and 0.25. According to Figure
24 5a, the Mach number contours at a jet pressure
25 ratio (PR) of 0.075 cause local disturbance in the
26 flow, creating a region with lower Mach numbers
27 around the injection point. This effect is relatively
28 small due to the low pressure ratio. In Figure 5b,

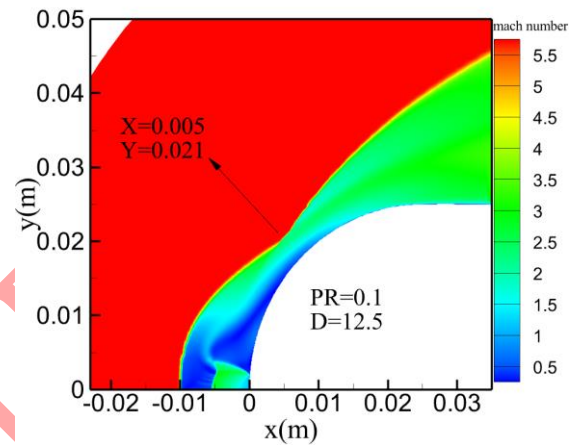
29 with an increased injection pressure (PR=0.1),
30 the disturbance in the flow is slightly more
31 significant than $PR = 0.075$. The region affected
32 by the jet expands, and a more noticeable
33 reduction in Mach numbers around the injection
34 point is observed. Figure 5c with PR=0.15 shows
35 a further increase in the jet's impact on the flow.

36 In this figure, the region with lower Mach
37 numbers enlarges, indicating stronger
38 interaction between the jet and the supersonic
39 flow. Figure 5d shows a greater effect of the high-
40 pressure jet on the flow, with the region of low
41 Mach numbers expanding. In Figure 5e, with PR =
42 0.25, the most significant disturbance in the flow
43 is observed, and the region with lower Mach

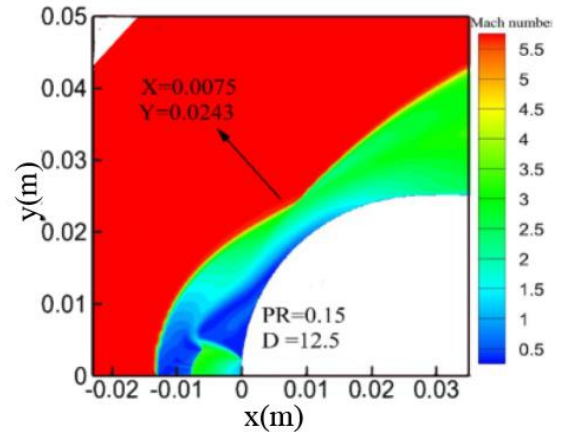
44 numbers has the largest area among all the
45 charts. Therefore, as the jet pressure ratio
46 increases from 0.075 to 0.25, the disturbance in
47 the Mach number contours increases, creating
48 larger regions of lower Mach numbers around the
49 injection point.



50 a) Jet Injection with Pressure Ratio 0.075



51 b) Jet Injection with Pressure Ratio 0.1

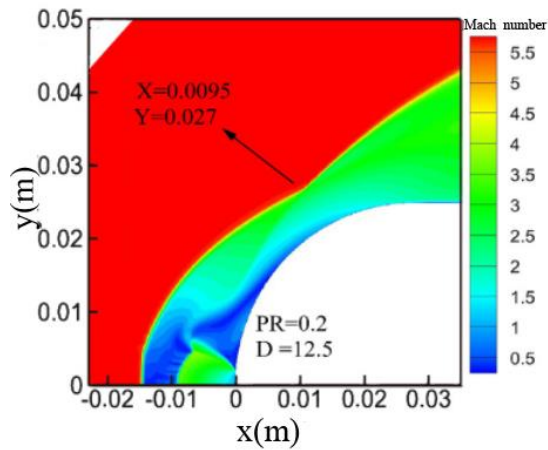


52 c) Jet Injection with Pressure Ratio 0.15

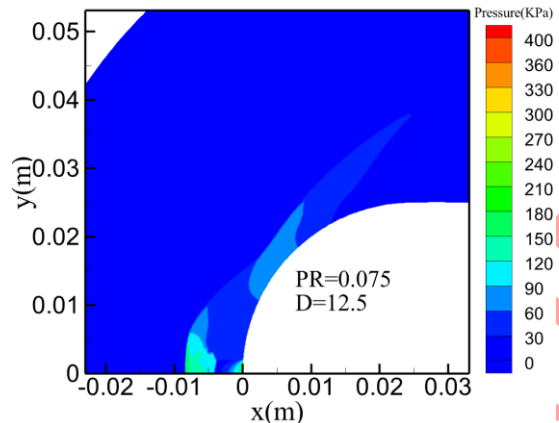
53
54
55

56
57
58

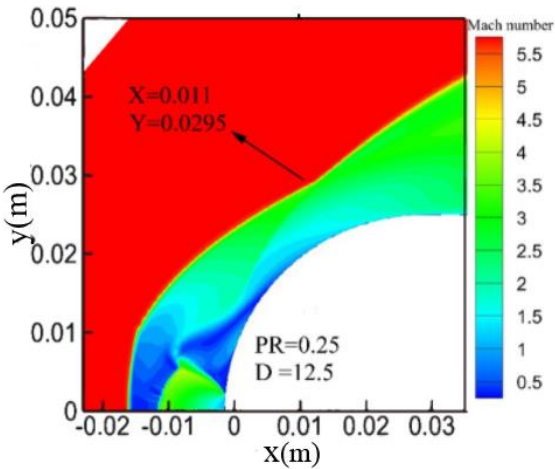
59
60
61



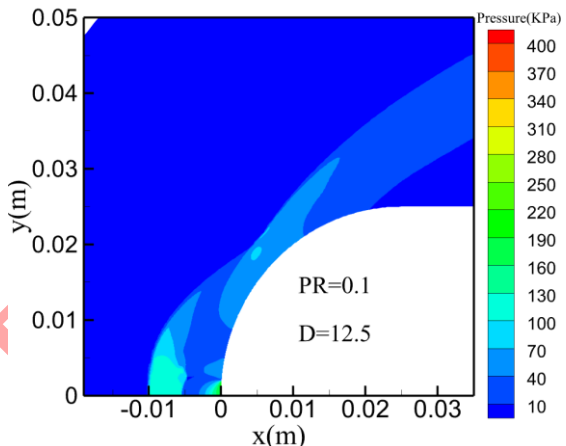
d) Jet Injection with Pressure Ratio 0.2



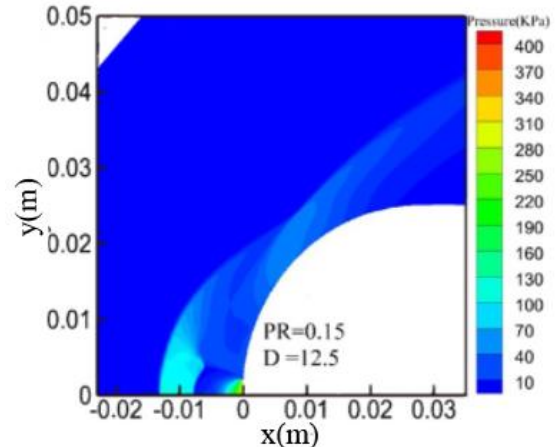
a) Jet Injection with Pressure Ratio 0.075



e) Jet Injection with Pressure Ratio 0.25



b) Jet Injection with Pressure Ratio 0.1



c) Jet Injection with Pressure Ratio 0.15

1
2

26
27

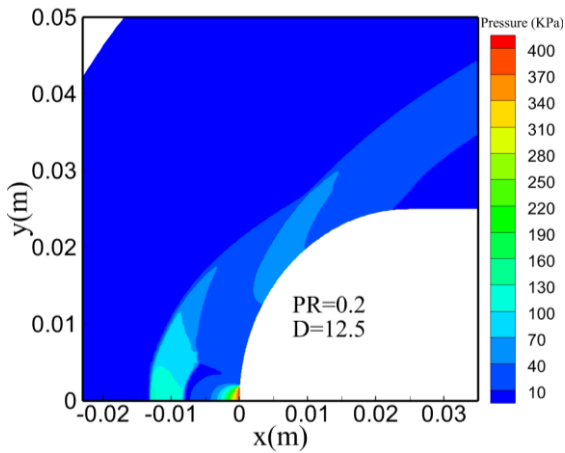
3
4

28
29

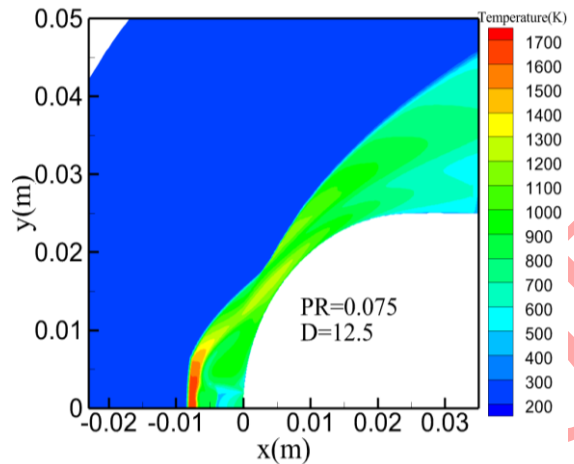
5 **Fig. 5.** Variations in Mach Number Contours at Injection
6 Pressure Ratios of 0.075, 0.1, 0.15, 0.2, and 0.25

7 Figure 6 shows that with an increase in jet
8 pressure ratio (PR) from 0.075 to 0.25, the static
9 pressure contours around the nose display
10 higher pressure regions and greater pressure
11 gradients, indicating stronger interactions
12 between the jet and the incoming flow with a
13 Mach number of 6. At low PR values, the jet's
14 influence is minimal, leading to small
15 disturbances and a shock wave close to the cone
16 surface. As PR increases, the high-pressure
17 region expands and the shock wave moves
18 further away from the cone. The highest jet
19 pressure ratio, PR=0.25 exhibits the most
20 significant disturbance in the flow field, marked
21 by a large high-pressure region and high-
22 pressure gradients. The jet's influence is
23 dominant at this stage, significantly altering the
24 shock wave structure and positioning it farther
25 from the nose

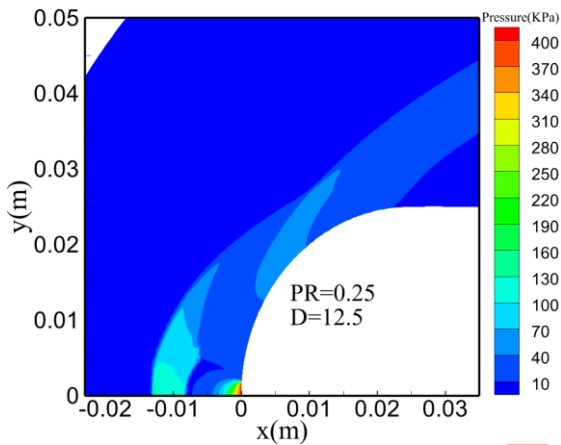
30
31
32



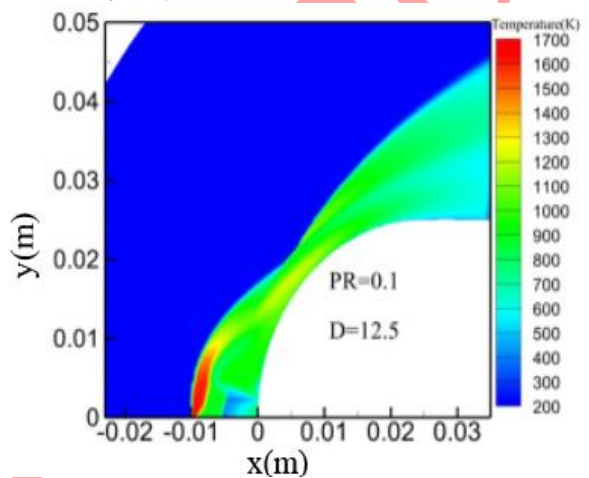
d) Jet Injection with Pressure Ratio 0.2



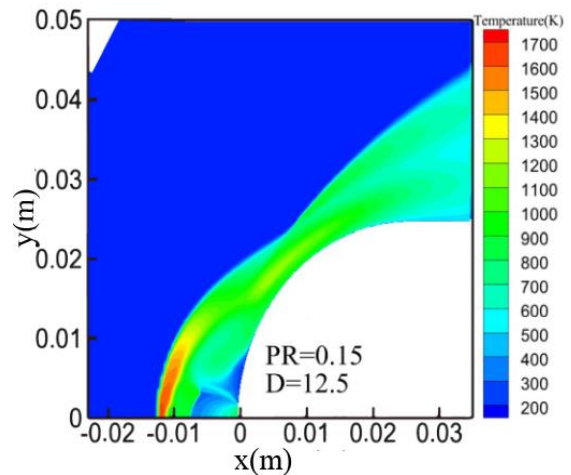
a) Jet Injection with Pressure Ratio 0.075



e) Jet Injection with Pressure Ratio 0.25



b) Jet Injection with Pressure Ratio 0.1



c) Jet Injection with Pressure Ratio 0.15

1
2

18
19

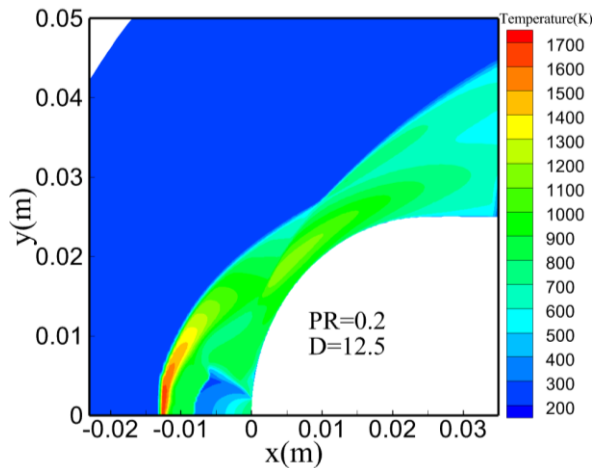
3
4

20
21

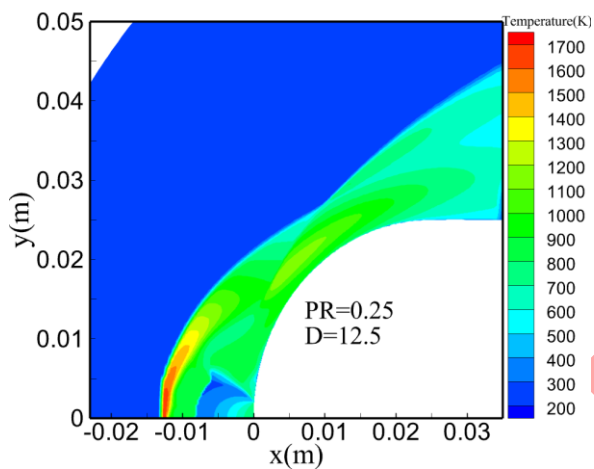
5 **Fig. 6.** Static Pressure Contours at Injection Pressure Ratios of
6 0.075, 0.1, 0.15, 0.2, and 0.25

7 By observing the static temperature contours
8 around the nose in Figure 7, it is seen that with an
9 increase in jet pressure ratio (PR) from 0.075 to
10 0.25, the high-temperature region moves farther
11 from the nose. Additionally, at the highest PR
12 (0.25), it is observed that the area of the high-
13 temperature region is the largest among all cases,
14 indicating the bow shock moving farther away
15 from the vehicle. Furthermore, the temperature
16 gradient in this case is higher than in the other
17 cases.

22
23



d) Jet Injection with Pressure Ratio 0.2



e) Jet Injection with Pressure Ratio 0.25

Fig. 7. Static Temperature Contours at Injection Pressure Ratios of 0.075, 0.1, 0.15, 0.2, and 0.25

Figure 8 shows the pressure variations on the body as a function of angle. It is observed that with an increase in the jet injection pressure ratio, the angle of the reattachment point of the flow to the body changes. In this case, the reattachment point angle changes from 37.5 to 39.2 degrees with an increase in pressure ratio. Moreover, according to Figures 8 and 9, the pressure and temperature at the reattachment point decrease with an increase in jet injection pressure ratio.

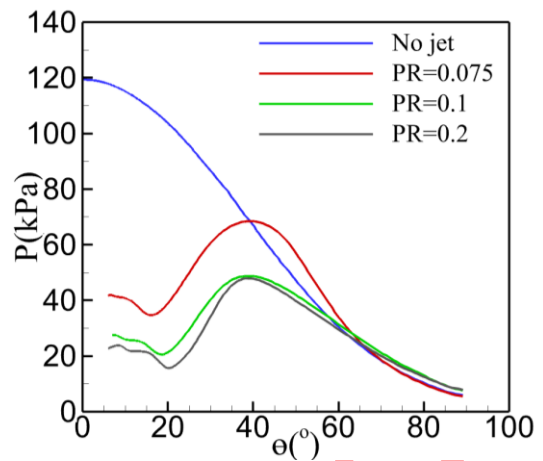
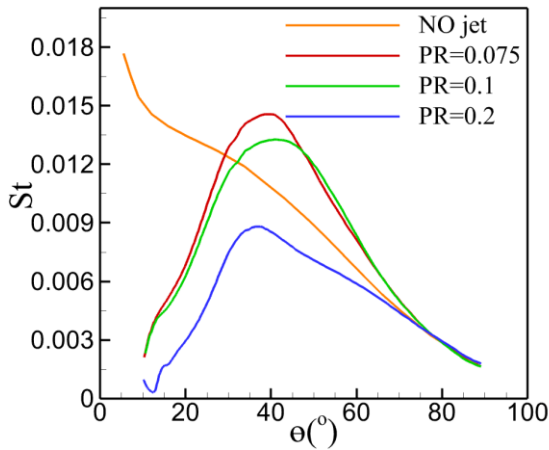


Fig. 8. Pressure Distribution on the Surface of the Geometry at Various Jet Injection Pressure Ratios

Based on the results of Figure 8, two phenomena can be stated. The first is that with an increase in jet injection pressure, the pressure in the upstream region of the injection point decreases. The second is that the pressure distribution after the flow reattachment point changes at higher injection pressure ratios compared to the case without injection. The high angle of the geometry in the figure above indicates that an increase in jet injection pressure significantly reduces the pressure in the front areas of the body but slightly increases the pressure in the rear areas of the geometry. Since the drag coefficient is highly dependent on the pressure in the front areas of the body, it is expected that an increase in jet injection pressure will reduce the drag coefficient. According to Figure 9, with an increase in jet injection pressure, the Stanton number decreases. A decrease in the Stanton number means that heat transfer between the wall and the fluid is reduced. In other words, the wall temperature is lower compared to the case without injection. Additionally, the angle at which the maximum Stanton number occurs decreases. This means that cooling is increased over a larger length of the nose.



1
2 **Fig. 9.** Distribution of Stanton Number on the Surface of the
3 Geometry at Various Jet Injection Pressure Ratios

4 Table 3 presents the results of the drag
5 coefficient, percentage reduction, heat transfer
6 rate, and mass flow rate of the jet injection at
7 various injection pressures. It is observed that
8 the increase in injection pressure has been able
9 to reduce the drag coefficient by 49.2%.

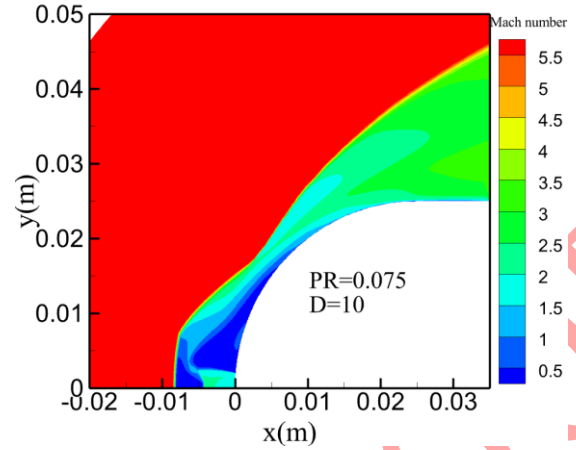
10 **Table 3.** Drag coefficient, heat transfer, and mass flow rate
11 increase with the rise in jet injection pressure.

Injection Press. (kPa)	(PR)	C_D	C_D Reduction (%)	H (kW/m ²)	\dot{m}_j (kg/s)
0 (benchmark)	0	0.8902	---	4.48	0
301.5	0.075	0.7299	18	3.0458	0.0048
402	0.1	0.6761	24	2.9577	0.0064
603	0.15	0.5511	38	2.1236	0.0096
804	0.2	0.4928	44.7	2.0079	0.0129
1005	0.25	0.4518	49.2	1.7915	0.0161

12

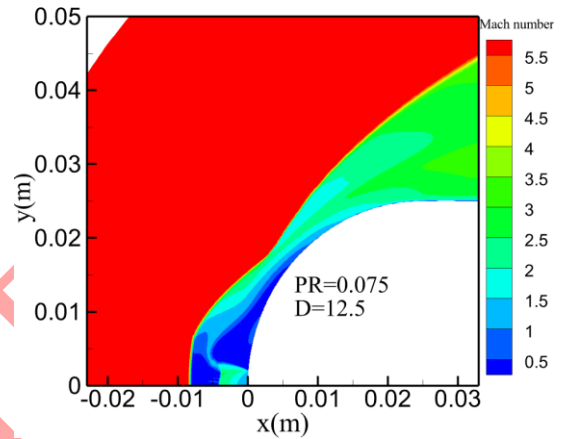
13 4.2. Jet Injection Diameter Investigation

14 To investigate the effect of the injection hole
15 diameter, the jet injection pressure is considered
16 to be 301.5 kPa, and the free stream Mach
17 number is 6. Only the effect of changing the jet
18 hole diameter with ratios of 10 and 12.5 is
19 examined. In Figure 10, the Mach number
20 distribution contour for the two simulated cases
21 with diameter ratios of 10 and 12.5 is shown.
22 With the increase in jet injection diameter, the
23 area affected by the injection becomes larger, and
24 the interaction between the curved shock wave
25 and the reflected shock wave from the surface is
26 not formed. Additionally, this increase in
27 diameter results in a higher mass flow rate of the
28 jet injection, leading to a greater distance of the
29 curved shock wave from the surface.



30
31

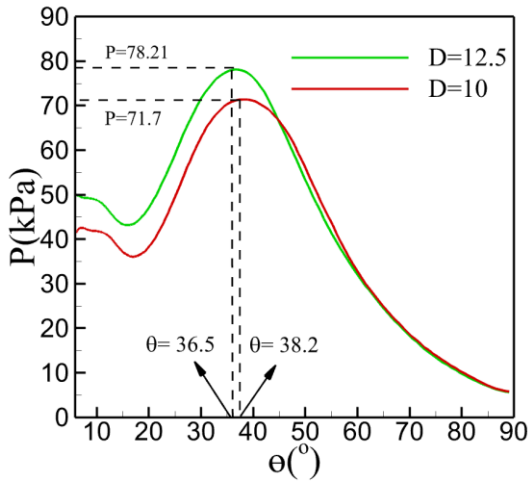
a) Pressure Ratio 0.075 and D=10



b) Pressure Ratio 0.075 and D=12.5

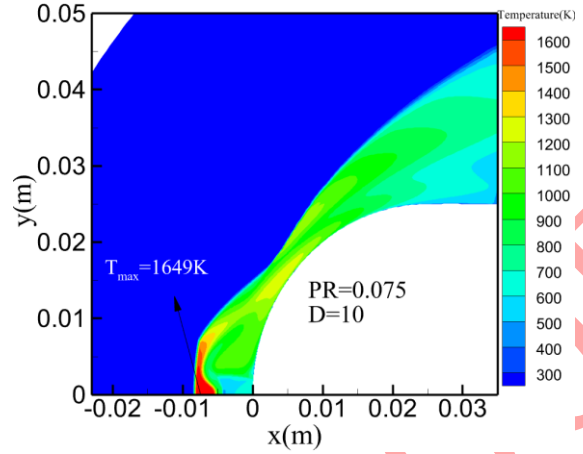
32
33 **Fig. 10.** Mach Number Contour at Injection Diameter Ratios
34 of 10 and 12.5

35 Figure 11 shows the pressure distribution on the
36 surface as a function of angle. It is observed that
37 the maximum pressure for the case with an
38 injection diameter ratio of 12.5 is 78.21 kPa, and
39 for the case with an injection diameter ratio of 10,
40 it is 71.7 kPa. Additionally, the increase in
41 injection diameter causes the maximum pressure
42 to occur at smaller angles on the surface, such
43 that for the ratio of 12.5, the maximum pressure
44 occurs at an angle of 36.5 degrees, and for the
45 ratio of 10, it occurs at an angle of 38.2 degrees.
46 This indicates that an increase in diameter leads
47 to a more uniform distribution of pressure on the
48 surface.
49



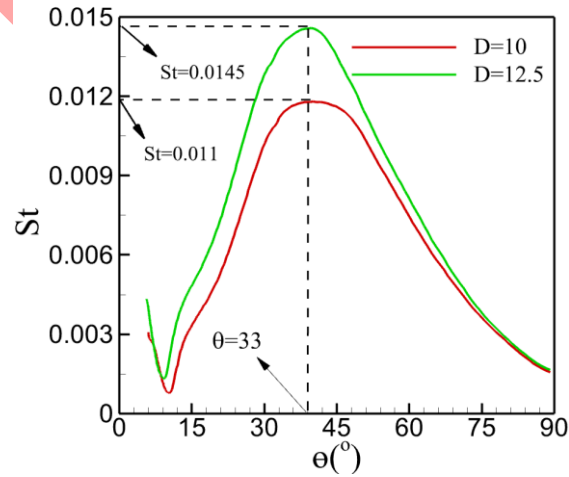
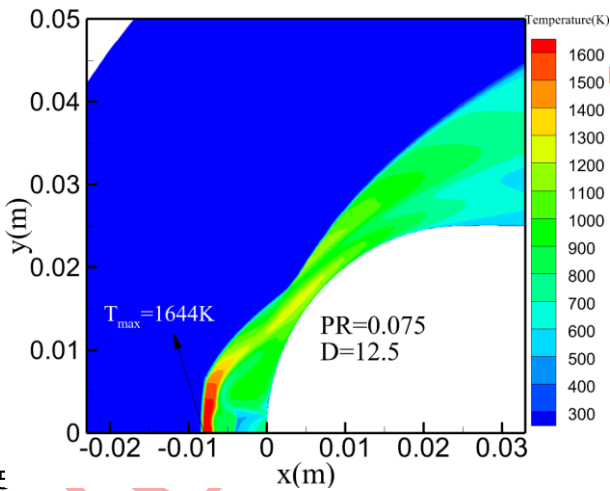
1
2 **Fig. 11.** Static Pressure Distribution on the Surface of the Body
3 at Diameter Ratios of 10 and 12.5

4 The temperature contours for the two diameter
5 ratios of 10 and 12.5 are depicted in Figure 12.
6 The maximum temperature for the cases with
7 injection diameter ratios of 10 and 12.5 are 1649
8 K and 1644 K, respectively. Additionally, the x-
9 coordinates of these maximum temperature
10 points for the injection diameters of 10 and 12.5
11 are -0.006 m and -0.0074 m, respectively. It is
12 observed that the higher injection diameter
13 results in a reduction of the maximum
14 temperature within the solution domain.



18
19 **Fig. 12.** Static Temperature Contour at Injection Diameter
20 Ratios of 10 and 12.5

21 According to Figure 13, the maximum Stanton
22 number for diameter ratios of 10 and 12.5 is
23 0.011 and 0.0145, respectively. It is observed that
24 with an increase in injection diameter, the
25 Stanton number decreases. This means that wall
26 heat transfer is reduced, and due to the constant
27 free stream air temperature, the wall
28 temperature consequently decreases. Therefore,
29 an increase in jet diameter leads to a reduction in
30 wall temperature.



31
32 **Fig. 13.** Distribution of Stanton Number at Injection Diameter
33 Ratios of 10 and 12.5

34 Table 4 shows that the drag coefficient decreases
35 with an increase in jet hole diameter. It is also
36 observed that with an increase in the mass flow
37 rate of the jet injection, both the drag coefficient
38 and heat transfer decrease. However, providing
39 this high mass flow rate for a long period requires
40 very large equipment and space. Therefore,
41 beyond a certain point, increasing the mass flow
42 rate is not feasible for practical use.

43

Table 4. Results of Drag Coefficient and Percentage Reduction with Increasing Jet Hole Diameter

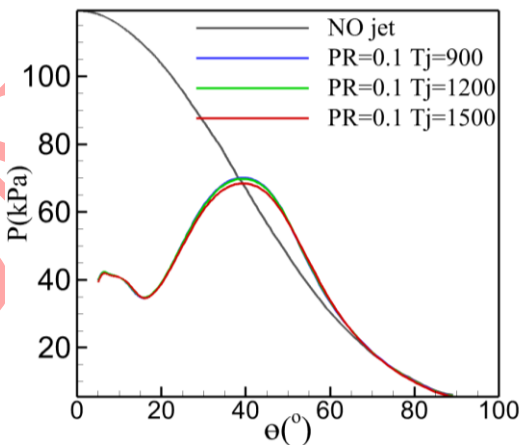
d_j (mm)	D(Di a. Ratio)	C_D	C_D Reductio n (%)	H (kW/m ²)	\dot{m}_j (kg /s)
0	---	0.89	---	4.48	---
4	12.5	0.73	18	3.0458	0.0048
5	10	0.68	23	2.6546	0.0075

3

4.3. Investigation of Injection Jet Temperature

5 Three jet injection temperatures of 900 K, 1200 K, and 1500 K were considered. In all these 6 K, and 1500 K were considered. In all these 7 temperatures, the injection pressure ratio is 0.1 8 and the diameter ratio is 12.5. Based on the 9 simulation results, the distribution of static 10 pressure and the Stanton number on the 11 geometry surface are shown in Figure 14. 12 According to Figure 14-a, it is observed that with 13 an increase in jet temperature at a constant 14 pressure ratio, the pressure distribution on the 15 surface does not change significantly. Only in the 16 reattachment region there is a slight increase in 17 pressure, which is negligible. Therefore, it can be 18 concluded that changing the jet temperature has 19 little effect on the pressure distribution on the 20 surface and consequently on the drag coefficient. 21 Table 7 presents the results of the drag coefficient 22 and percentage changes with the increase in jet 23 injection temperature, which confirms the 24 negligible changes in drag with jet temperature. 25 Figure 14-b shows the variations in the Stanton 26 number on the surface of the nose. It is observed 27 that the lower the jet injection temperature, the 28 lower the Stanton number. This means that jet 29 injection at a lower temperature leads to 30 improved cooling of the nose. Additionally, 31 quantitatively, the heat flux values for jet 32 injection at different temperatures are 33 mentioned in Table 5.

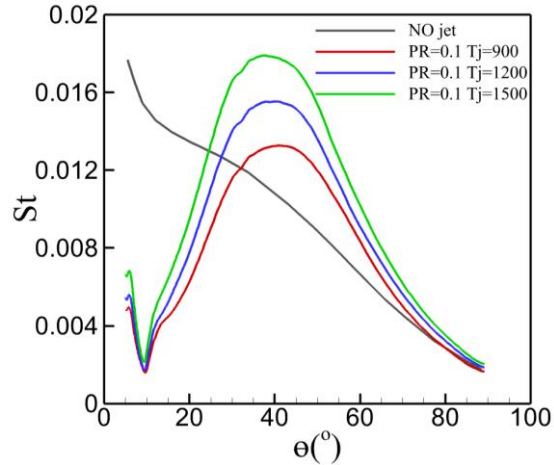
34



35

36

a) Pressure Variations



37
38

b) Stanton Number Variations

Fig. 14. Variations in Pressure and Stanton Number on the Surface of the Nose at Injection Temperatures of 900 K, 1200 K, and 1500 K

39

Table 5. Results of Drag Coefficient and Percentage Reduction with Increasing Stagnation Temperature of Jet Injection

$T_{0,j}$ (K)	C_D	C_D Reductio n (%)	H (kW/m ²)	\dot{m}_j (kg /s)
0	0.89	---	4.48	---
900	0.6762	24	2.96	0.0064
1200	0.6842	23	3.4	0.0055
1500	0.6837	23.2	3.86	0.0049

40

41

42

43

44

45

46

47

48

49

50

51

52

53

54

55

56

57

58

59

60

61

62

63

64

65

66

67

68

69

70

71

72

73

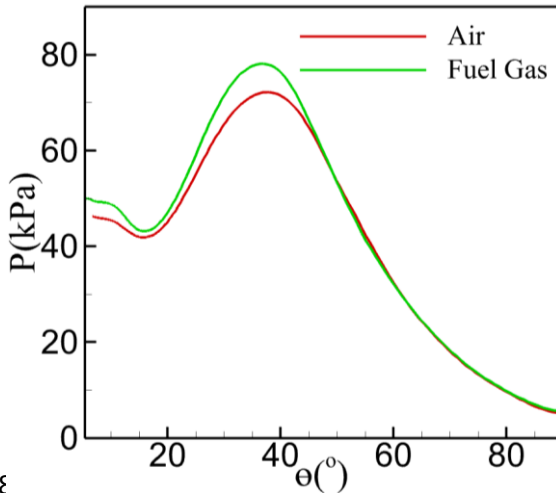
74

4.4. Investigation of the Injected Fluid Material

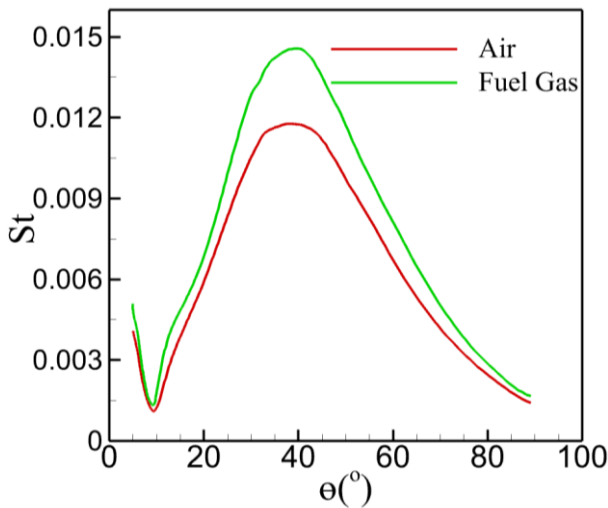
Another important parameter in the issue of drag reduction using jet injection is the type of injected fluid. Changing the fluid properties alters certain physical behaviors, such as the penetration and dispersion of the injected fluid. Accordingly, the effects of two injection fluids, air and a composite gas or fuel gas (N_2O), will be examined. This study is conducted at a pressure ratio of 0.075, a jet temperature of 900 K, and a diameter ratio of 12.5. In Figure 15-a, the pressure distribution for the two injection fluids is shown. The pressure on the surface from the jet injection area to before the reattachment point is lower with air injection compared to the composite gas case; such that at the angle of maximum surface pressure, 37.5 degrees, air injection achieves 7.5% less pressure than composite gas injection.

The results of the Stanton number distribution on the surface for these two different fluids are shown in Figure 15-b. By changing the injection fluid from composite gas to air, the Stanton number at its maximum value decreases by approximately 19.3%. Unlike the static pressure distribution, where the pressure of the two fluids equalizes downstream of the maximum

1 pressure point, the Stanton number is higher for
 2 the composite gas than for the injected air. In
 3 other words, changing the injection fluid affects
 4 the overall surface heat transfer but only
 5 changes the surface pressure up to the
 6 maximum surface pressure area and slightly
 7 downstream of it.



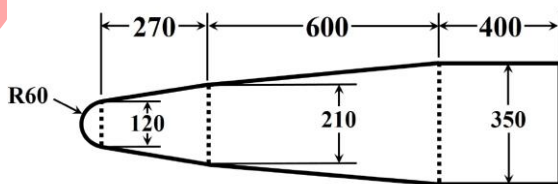
9 a) Pressure Distribution on the Surface of the Nose



11 b) Distribution of Stanton Number on the Surface of the Nose
 12 Fig. 15: Variations in Pressure and Stanton Number for the
 13 Injection of Two Different Fluids

14 4.5. Double Cone Geometry Without Jet 15 Injection

16 The innovation of this paper lies in considering a
 17 double cone geometry for the nose. The studied
 18 geometry along with its dimensions is presented
 19 in Figure 16.



20

21 Fig. 16. Double Cone Geometry (Dimensions are in
 22 Millimeters)

23 For the numerical simulation of the double cone
 24 geometry, a structured grid is used. The
 25 numerical simulation of this geometry is also
 26 performed using Fluent software, with the
 27 previous general settings and the far-field flow
 28 conditions according to Table 6.

29 Table 6. Far-Field Flow Conditions for Double Cone Geometry

Freestream Mach Number	4.5
Freestream Static Pressure (kPa)	41.06
Freestream Static Temperature (K)	242

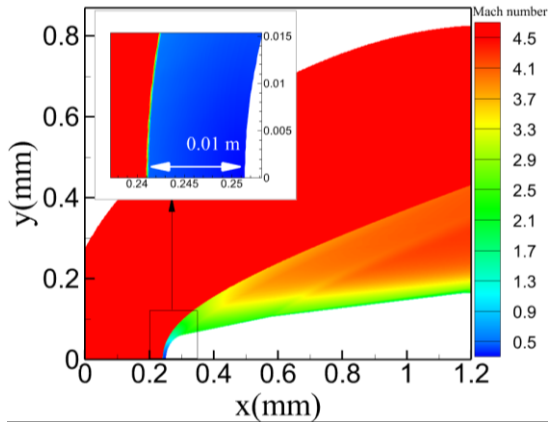
30 Accordingly, the stagnation pressure and
 31 temperature in the freestream are calculated to
 32 be approximately 1091 bar and 1220 K,
 33 respectively. The independence of the structured
 34 computational grid in the absence of jet injection
 35 was examined in three grids with 182,000,
 36 282,000, and 370,000 cells. The results of the
 37 drag coefficient and surface heat transfer for
 38 these three grids are shown in Table 7.

40 Table 7. Grid Independence Results for Double Cone
 41 Geometry

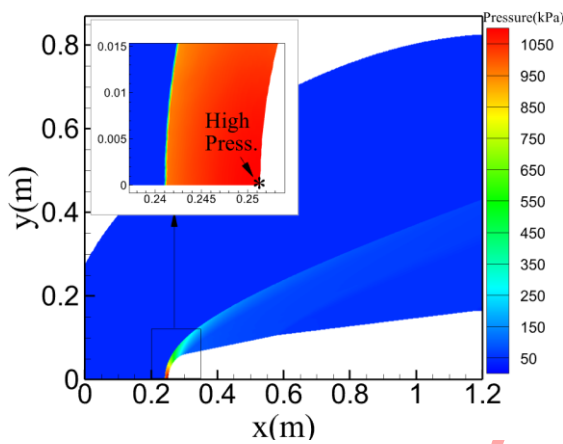
#	No. grid	C_D	H (kW/m ²)
Coarse	182380	0.1666	506311
Standard	282660	0.1679	542372
fine	370150	0.1680	540687

43 Based on the results of Table 7, the changes in the
 44 drag coefficient and surface heat flux from the
 45 standard grid compared to the fine grid are
 46 0.06% and 0.31%, respectively. The change in the
 47 drag coefficient in the coarse grid is
 48 approximately 0.7%, which is acceptable, but due
 49 to the 1.7% change in heat flux, the standard grid
 50 is used as the reference grid in the rest of the
 51 article.

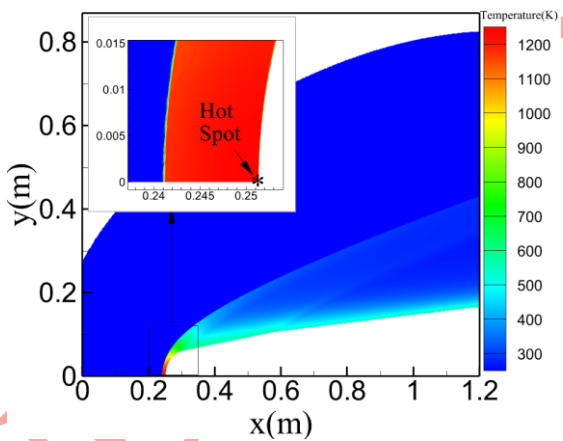
52 The contours of the Mach number, static
 53 pressure, and static temperature are shown in
 54 Figure 18.



1
2 a) Mach Number Contour in Double Cone Geometry Without
3 Jet Injection



4
5 b) Static Pressure Contour in Double Cone Geometry Without
6 Jet Injection



7
8 c) Temperature Contour in Cone Geometry Without Jet
9 Injection

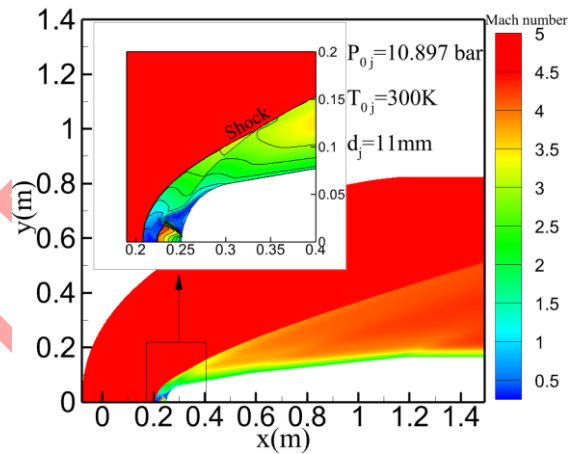
10 **Fig. 17.** Static Temperature Contour in Double Cone Geometry
11 Without Jet Injection
12 Considering the contours presented for the case
13 without jet injection, it is observed that the most
14 significant changes occur at the front of the nose.
15 According to Figure 18-a, the minimum distance
16 of the bow shock from the nose is equal to 10
17 millimeters. Additionally, Figure 18-b shows that
18 the maximum pressure value is 1091 kilopascals
19 and occurs at the stagnation point in the center of
20 the nose. Figure 18-c also shows the maximum

21 temperature at the stagnation point on the nose,
22 and its value is 1225 K.

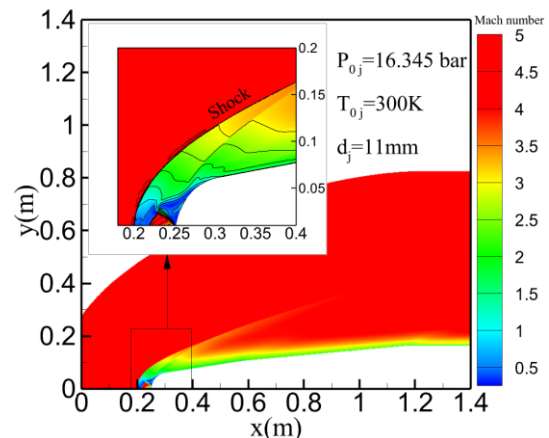
23

24 4.6. Investigation of the Effect of Jet Pressure 25 Ratio in Double Cone Geometry

26 To investigate the effect of the jet injection
27 pressure parameter on drag and heat reduction
28 in this geometry using numerical simulation,
29 three values of 10.897, 16.345, and 21.793 bar at
30 a jet hole diameter of 11 millimeters are
31 examined. Considering the freestream stagnation
32 pressure (i.e., 118.5 bar), the three dimensionless
33 injection pressure ratios are 0.092, 0.138, and
34 0.184, respectively, similar to the values studied
35 in the hemispherical geometry (Figure 19). For
36 the three aforementioned pressure ratios, the
37 bow shock forms at distances of 44, 52, and 59
38 millimeters.

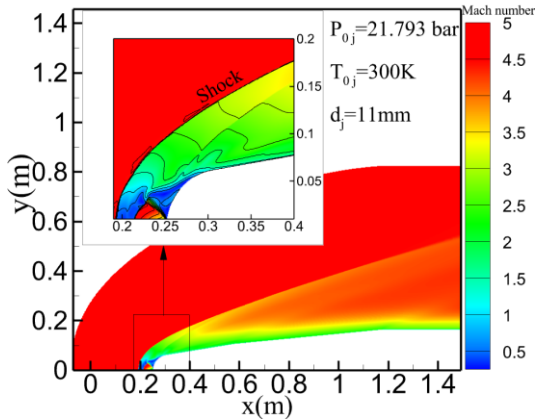


a) Injection Pressure Ratio 0.092



b) Injection Pressure Ratio 0.138

42
43



c) Injection Pressure Ratio 0.184

Fig. 18. Mach Number Contour in Double Cone Geometry for Various Jet Injection Pressures

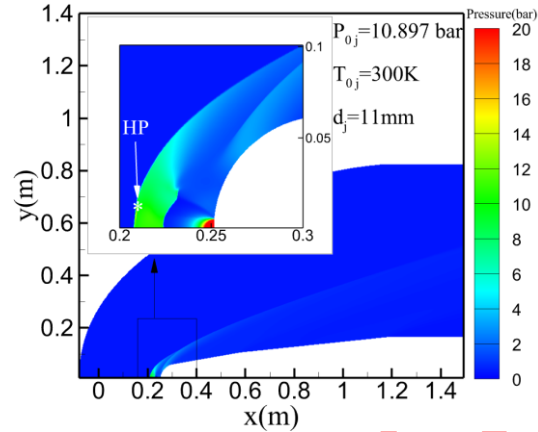
The values of the drag coefficient and heat flux are presented in Table 8. The results show that increasing the injection pressure for the double cone geometry leads to a reduction in the drag coefficient. At an injection pressure ratio of 0.184, the drag coefficient is reduced by 62.7% compared to the baseline case (without injection). Additionally, the heat transfer rate also decreases at an injection pressure ratio of 0.184, indicating that increasing the injection pressure leads to more effective cooling of the nose.

Table 8. Change in Drag Coefficient and Heat Flux of Double Cone Geometry with Increased Jet Injection Pressure

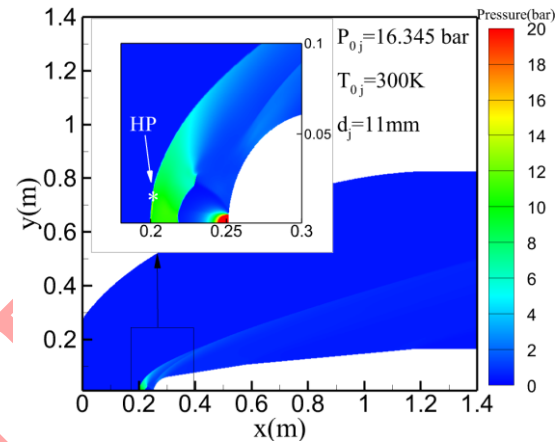
Injection Press. (kPa)	(PR)	C_D	C_D Reduction (%)	H (kW/m ²)	\dot{m}_j (kg/s)
0 (benchmark)	0	0.1679	---	842.372	0
10.89	0.092	0.0865	48.5	412.708	2.33
16.34	0.138	0.071	57.7	406.974	3.49
21.79	0.184	0.0627	62.7	318.040	4.66

20

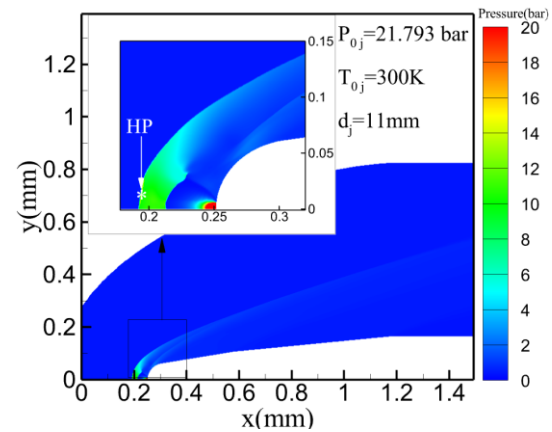
In Figure 18, it can be seen that with the increase in jet injection pressure, the recompression wave generated by the injection combines with the curved shock wave of the geometry, and the pressure at the reattachment point decreases. The maximum static pressure after the shock, in the case of an injection pressure of 10.897 bar, is 14.28 bar. Also, for the injection pressure of 16.345 bar, the pressure after the shock is 14.70 bar, and for the injection pressure of 21.793 bar, it is 15.62 bar.



a) Static Pressure Contour at 10.897 Bar Jet Injection Pressure



b) Static Pressure Contour at 16.345 Bar Jet Injection Pressure



c) Static Pressure Contour at 21.793 Bar Jet Injection Pressure

Fig. 19. Static pressure Contour in Double Cone Geometry for Various Jet Injection Pressures

36

37

38

39

40

41

42

43

44

45

46

47

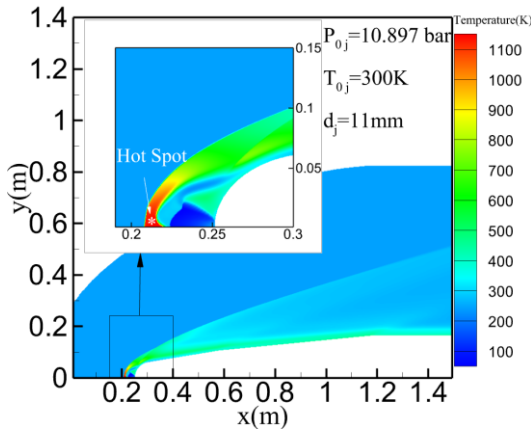
48

49

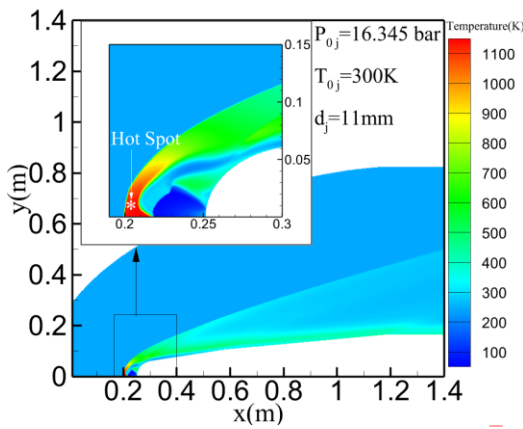
50

With the increase in injection pressure, it is expected that the temperature around the nose of the geometry will decrease. Figure 19 clearly shows that with the increase in the injection pressure ratio, the area of the cold region resulting from the injection becomes larger. However, it should be noted that with the increase in jet injection pressure, the temperature after the shock, which is the region with the highest temperature, for injection

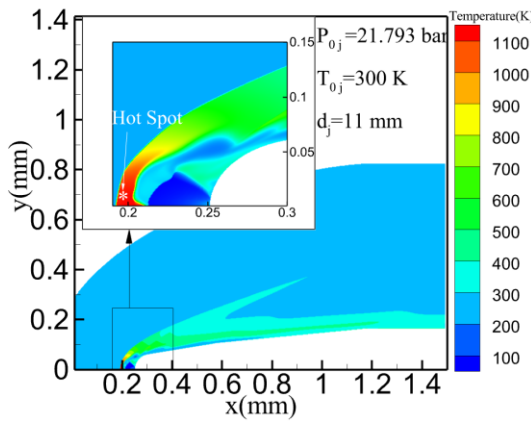
1 pressures of 10.897, 16.345, and 21.793 bar is
 2 1160.2 K, 1159.4 K, and 1153.5 K, respectively.



3



4



5

6 **Fig. 20.** Static Temperature Contour in Double Cone
 7 Geometry for Various Jet Injection Pressures

8

9 4.7. Investigation of the Effect of Jet Diameter 10 in Double Cone Geometry

11 To investigate the effect of jet injection diameter
 12 in this geometry, simulations were evaluated for
 13 three diameters: 11 mm, 13.2 mm, and 16.5 mm
 14 at an injection pressure of 21.79 bar. According to
 15 Table 9, as the jet injection diameter increases,
 16 the drag coefficient decreases and the mass flow
 17 rate increases. The percentage reduction in drag
 18 coefficient for the sample with the largest jet

19 injection diameter is 75.04%, which is a
 20 significant value.

21

22

23

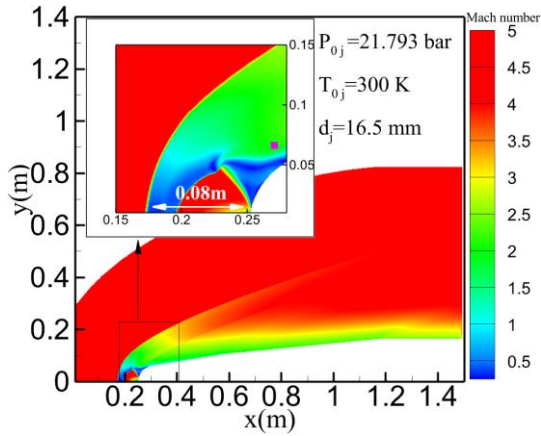
Table 9. Results of Changes in Drag Coefficient and Heat Flux
 of Double Cone Geometry with Increased Jet Hole Diameter

d_j (mm)	D(Di a. Ratio)	C_D	C_D Reductio n (%)	H (kW/m ²)	\dot{m}_j (kg /s)
0	---	0.1679	---	542.372	---
16.5	20	0.0419	75.04	308.468	10.485
13.2	25	0.0522	68.9	290.444	6.71
11	30	0.0627	62.7	318.040	4.66

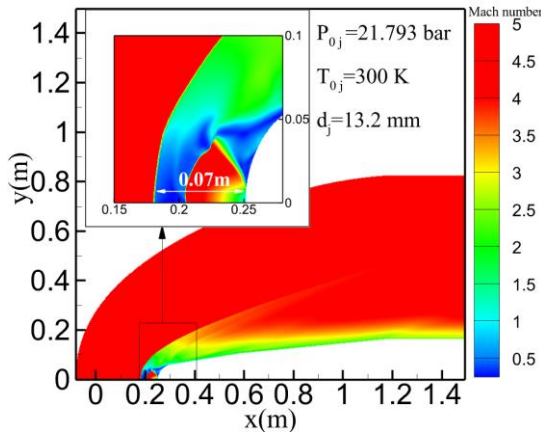
24

25

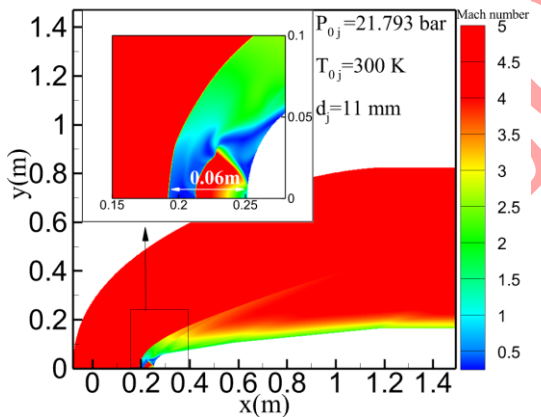
26 In Figure 20, the Mach number contour for three
 27 different jet diameter ratios is presented.
 28 According to the obtained results, the distances of
 29 the curved shock wave in front of the geometry
 30 for increasing jet hole diameters are 58, 69, and
 31 78 millimeters, respectively; this indicates that
 32 the wave moves further away from the nose of
 33 the geometry as the jet hole diameter increases.
 34 Additionally, by comparing Table 8 and Table 9, it
 35 is observed that with an increase in mass flow
 36 rate from approximately 2.3 to 4.6 kilograms per
 37 second (increased injection pressure), the
 38 percentage reduction in the drag coefficient
 39 changes by 14 units (from 48 to 62). However,
 40 with an increase in mass flow rate from 4.6 to
 41 10.5 kilograms per second (increased injection
 42 diameter), the percentage reduction in the drag
 43 coefficient changes by 13 units (from 62 to 75). In
 44 other words, operationally, using a smaller jet
 45 hole with higher injection pressure is more
 46 efficient, as it achieves suitable drag and heat flux
 47 reduction with lower mass flow consumption.



1



2



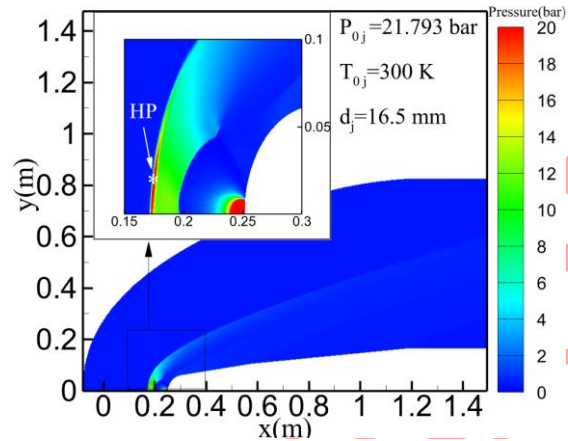
3

4 **Fig. 21.** Mach Number Contour in Double Cone Geometry for
5 Various Jet Injection Diameters

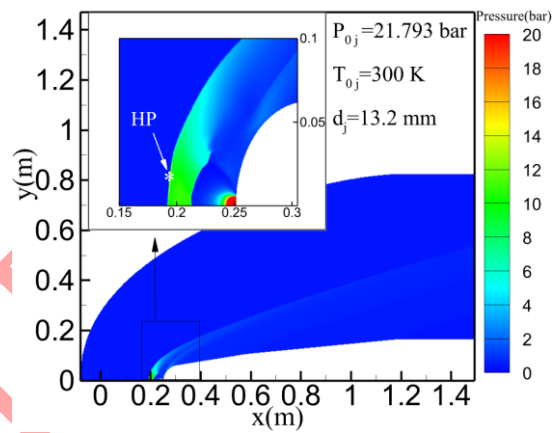
6

7 Figure 21 shows the pressure contour for
8 different jet injection diameters. The results
9 indicate that the pressure after the shock
10 formation area increases with the increase in the
11 jet injection diameter. The pressure values for jet
12 injection diameters of 11 mm, 13.2 mm, and 16.5
13 mm are 15.96 bar, 16.07 bar, and 19.3 bar,
14 respectively. The injection pressure in all three
15 cases is 21.793 bar. This indicates that the
16 increase in injection pressure leads to the
17 formation of a stronger bow shock upstream of
18 the nose. However, at the same time, the distance

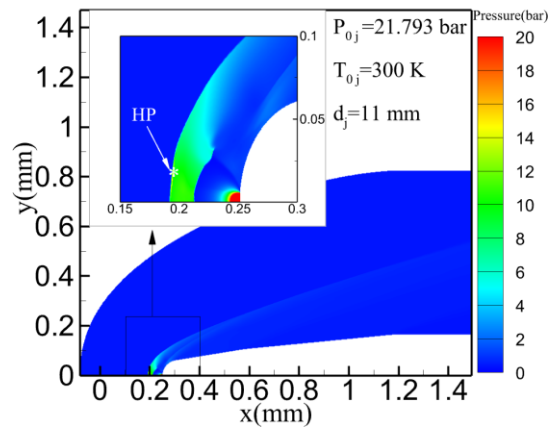
19 of the shock from the nose increases with the
20 increase in injection pressure.



21



22



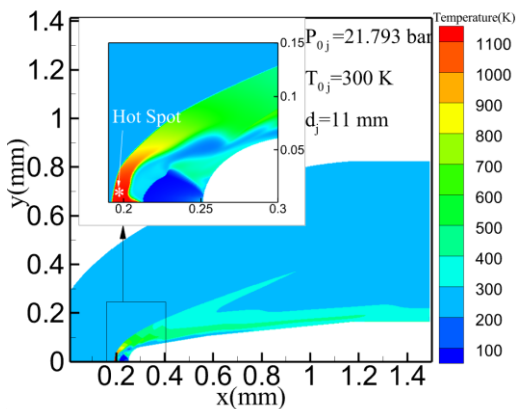
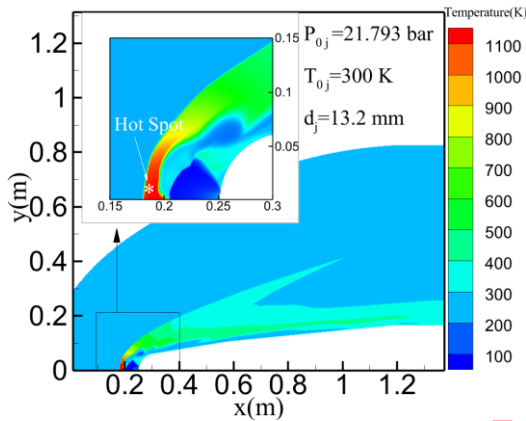
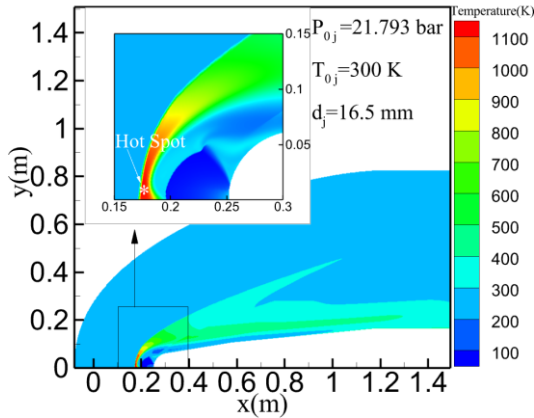
23

24 **Fig. 22.** Static Pressure Contour in Double Cone Geometry for
25 Various Jet Injection Diameters

26

27 According to Figure 22, which shows the
28 temperature distribution of the double cone
29 geometry for different jet injection diameters
30 (16.5 mm, 13.2 mm, and 11 mm), the maximum
31 temperature values for these diameters are
32 1148.1 K, 1152.1 K, and 1153.9 K, respectively.
33 Therefore, it can be concluded that with the
34 increase in jet injection diameter, the maximum
35 temperature at the front of the nose (shock
formation area) decreases. Additionally, it

1 should be noted that the injection temperature
 2 for all three cases is 300 K.



6 **Fig. 23.** Static Temperature Contour in Double Cone Geometry
 7 for Various Jet Injection Diameters

8 5. Conclusions

9 This study analyzed the effects of jet injection on
 10 drag reduction and heat transfer control for
 11 single-cone and double-cone nose geometries in
 12 hypersonic flow conditions. The results
 13 demonstrated that increasing the jet injection
 14 pressure significantly reduces aerodynamic drag,
 15 with reductions of 49.2% for the single-cone

16 geometry and 62.7% for the double-cone
 17 geometry. Additionally, increasing the injection
 18 diameter further enhances drag reduction,
 19 reaching 75.04% for the double-cone case with a
 20 16.5 mm injection diameter. The findings also
 21 indicate that jet injection shifts the bow shock
 22 upstream, reducing stagnation pressure and
 23 temperature, which helps in thermal
 24 management. Furthermore, using alternative
 25 injection gases, such as gas mixtures instead of
 26 air, lowered the maximum Stanton number by
 27 19.3%, further enhancing heat transfer control.
 28 Beyond a certain injection pressure, the
 29 improvement in drag reduction becomes
 30 minimal, and the primary benefit transitions to
 31 heat reduction. The study confirms that
 32 optimizing jet injection parameters—such as
 33 pressure ratio, injection diameter, and injected
 34 fluid properties—is essential for balancing drag
 35 reduction and thermal protection in hypersonic
 36 applications. Future research can explore the
 37 combined effects of jet injection with other flow
 38 control techniques, such as aerospikes or energy
 39 discharge methods, to enhance aerodynamic
 40 efficiency further. In general The results indicate
 41 that increasing the jet injection pressure ratio is
 42 the most effective method for reducing drag. The
 43 most effective method for reducing the Stanton
 44 number and thereby minimizing heat transfer is
 45 increasing the injection temperature, while the
 46 best approach for lowering the temperature near
 47 the device is optimizing the jet diameter and
 48 injection pressure.

49 While this study provides insights into the effects
 50 of jet injection on drag and heat transfer in
 51 hypersonic flows, several avenues for future
 52 research can further advance this field including:
 53 combination with other flow control Techniques,
 54 unsteady flow analysis, optimization of Injection
 55 parameters, thermal and structural analysis,
 56 alternative injection gases and mixtures, and
 57 studying and simulation of three-dimensional
 58 effects:

59 Nomenclature

H	Specific enthalpy [kJ/kg]
I	Exergy destruction rate [kJ/kg]
M	Mass flow rate [kg/s]
P	Pressure [bar]

60

61

Conflicts of Interest

There are no conflicts of interest for this research.

References

- [1]. Fadgyas, M., et al. Fast computational hypersonic heat flux estimation. in AIP Conference Proceedings. 2018. AIP Publishing.
- [2]. Natali, M., J.M. Kenny, and L. Torre, Science and technology of polymeric ablative materials for thermal protection systems and propulsion devices: A review. *Progress in Materials Science*, 2016. 84: p. 192-275.
- [3]. Huang, W., A survey of drag and heat reduction in supersonic flows by a counterflowing jet and its combinations. *Journal of Zhejiang University-Science A*, 2015. 16(7): p. 551-561.
- [4]. Zhou, C. and W. Ji, A three-dimensional numerical investigation on drag reduction of a supersonic spherical body with an opposing jet. *Proceedings of the Institution of Mechanical Engineers, Part G: Journal of Aerospace Engineering*, 2014. 228(2): p. 163-177.
- [5]. Guo, J., et al., Parametric study on the heat transfer of a blunt body with counterflowing jets in hypersonic flows. *International Journal of Heat and Mass Transfer*, 2018. 121: p. 84-96.
- [6]. Xiwan, S., et al., A survey on numerical simulations of drag and heat reduction mechanism in supersonic/hypersonic flows. *Chinese Journal of Aeronautics*, 2019. 32(4): p. 771-784.
- [7]. Ganesh, M.A. and B. John, Concentrated energy addition for active drag reduction in hypersonic flow regime. *Acta astronautica*, 2018. 142: p. 221-231.
- [8]. Lekzian, E., Study of a non-reacting hypersonic flow over an external cavity with flow injection using DSMC method. *Aerospace Science and Technology*, 2023. 140: p. 108492.
- [9]. Huang, W., et al., Drag and heat flux reduction mechanism induced by the spike and its combinations in supersonic flows: A review. *Progress in Aerospace Sciences*, 2019. 105: p. 31-39.
- [10]. Darbandi, M., Lakzian, E. Mixing enhancement of two gases in a microchannel using DSMC. in *Applied Mechanics and Materials*. 2013. Dubai: Trans Tech Publ.
- [11]. Darbandi, M., M. Sabouri, E. Lekzian, and G.E. Schneider. A Direct Simulation Monte Carlo Study on the Effect of Temperature Gradient on the Gas Mixing in Microgeometries. in *11th International Energy Conversion Engineering Conference*. 2013.
- [12]. Lekzian, E. and H.R. Farshi Fasih, Effect of Obstacles Location and Flow Injection on the Mixing of Two-Gaseous Flow in a Microchannel. *Amirkabir Journal of Mechanical Engineering*, 2022. 54(9): p. 2139-2156.
- [13]. Lekzian, E. and M. Sabouri, DSMC investigation on rarefied gas mixing through diverging and converging channels. *International Communications in Heat and Mass Transfer*, 2024. 157: p. 107764.
- [14]. Lekzian, E., A. Ebrahimi, and H. Parhizkar, Performance analysis of microelectromechanical thrusters using a direct simulation Monte Carlo solver. *Proceedings of the Institution of Mechanical Engineers, Part G: Journal of Aerospace Engineering*, 2017. 232(7): p. 1212-1222.
- [15]. Lekzian, E., H. Parhizkar, and A. Ebrahimi, Study of the effects of preheated wall/plates in microthruster systems. *Journal of Theoretical and Applied Mechanics*, 2018. 56(3): p. 713-725.
- [16]. Guangming Guo, G., L. Qin, and J. Wu, Effect of opposing jet layouts on flow and aerodynamic heating characteristics in rarefied hypersonic flows over a blunt body, *Aerospace Science and Technology*, 2025, Vol. 158, 109891 (22 pages)
- [17]. Huang, J., W.-X. Yao, and Z.-P. Jiang, Penetration fine effect on thermal protection system by opposing jet. *Acta Astronautica*, 2019. 160: p. 206-215.
- [18]. Wang, Z. and X. Zhang, Parametric research on drag reduction and thermal protection of blunt-body with opposing jets of forward convergent nozzle in supersonic flows. *Acta Astronautica*, 2022. 190: p. 218-230.
- [19]. Jin, W., Attached flow formed by opposing jet in hyper/supersonic flow. *International Journal of Heat and Mass Transfer*, 2019. 141: p. 905-921.
- [20]. Yuan, Z., W. Zhao, and W. Chen. Numerical study of heat flux reduction mechanism of the

counterflowing jet in rarefied flows. in AIP Conference Proceedings. 2019. AIP Publishing.

[21]. Shen, B., W. Liu, and L. Yin, Drag and heat reduction efficiency research on opposing jet in supersonic flows. *Aerospace Science and Technology*, 2018. 77: p. 696-703.

[22]. Li, S.-b., et al., Research on the drag reduction performance induced by the counterflowing jet for waverider with variable blunt radii. *Acta Astronautica*, 2016. 127: p. 120-130.

[23]. Gerdroodbary, M.B., M. Imani, and D. Ganji, Investigation of film cooling on nose cone by a forward facing array of micro-jets in hypersonic flow. *International Communications in Heat and Mass Transfer*, 2015. 64: p. 42-49.

[24]. Yisheng, R., Drag reduction research in supersonic flow with opposing jet. *Acta Astronautica*, 2013. 91: p. 1-7.

[25]. Gerdroodbary, M.B., S. Bishehsari, S. Hosseinalipour, and K. Sedighi, Transient analysis of counterflowing jet over highly blunt cone in hypersonic flow. *Acta Astronautica*, 2012. 73: p. 38-48.

[26]. Chen, L.-W., G.-L. Wang, and X.-Y. Lu, Numerical investigation of a jet from a blunt body opposing a supersonic flow. *Journal of Fluid Mechanics*, 2011. 684: p. 85-110.

[27]. Anjalidevi, S. and S. Aruna, Effect of counterflow jet on attenuation of drag and aerodynamic heating over a coneogive body in hypersonic flow. *Applied Mathematics and Mechanics*, 2011. 7(4): p. 95-122.

[28]. Bilal Hussain Shah, S. and X.-Y. Lu, Computational study of drag reduction at various freestream flows using a counterflow jet from a hemispherical cylinder. *Engineering Applications of Computational Fluid Mechanics*, 2010. 4(1): p. 150-163.

[29]. Tamada, I., S. Aso, and Y. Tani. Reducing aerodynamic heating by the opposing jet in supersonic and hypersonic flows. in 48th AIAA Aerospace Sciences Meeting Including the New Horizons Forum and Aerospace Exposition. 2010.

[30]. Kulkarni, V. and K. Reddy, Effect of a supersonic counterflow jet on blunt body heat transfer rates for oncoming high enthalpy flow. *Journal of Engineering Physics and Thermophysics*, 2009. 82: p. 1-5.

[31]. Kulkarni, V. and K. Reddy. Drag reduction by counterflow supersonic jet for a blunt cone in high enthalpy flows. in *Shock Waves: 26th International Symposium on Shock Waves*, Volume 1. 2009. Springer.

[32]. Sriram, R. and G. Jagadeesh, Film cooling at hypersonic Mach numbers using forward facing array of micro-jets. *International journal of heat and mass transfer*, 2009. 52(15-16): p. 3654-3664.

[33]. Cheng, G., et al. Numerical study of flow augmented thermal management for entry and re-entry environments. in 25th AIAA Applied Aerodynamics Conference. 2007.

[34]. Hayashi, K., S. Aso, and Y. Tani. Numerical study of thermal protection system by opposing jet. in 43rd AIAA Aerospace Sciences Meeting and Exhibit. 2005.